Supporting Information

Wang et al. 10.1073/pnas.1014970108

SI Methods

Molecular Dynamics Simulations. Computer simulations are carried out with the LAMMPS molecular dynamics package (1) in NVT ensemble. The temperature (300 K) is maintained by Nose–Hoover thermostat (2) with 0.1-ps time constant, and the simulation time step is 1 fs with Verlet integrator. Lennard–Jones interactions are truncated smoothly at 11.0 Å, electrostatic interactions are treated by particle-particle-particle mesh solver (pppm) (3) with a real space cutoff of 11.0 Å, and precision tolerance of 10^{-5}. In view of the droplet's coexistence with its own vapor, pressure remains close to vapor pressure of water throughout the simulation. Simulation box contains extra space in z direction (300 Å) to minimize interactions with system's periodic images in z direction.

Water Contact Angle Calculations. We use water drops comprising 2,000 Extended Simple Point Charge model (SPC/E) (4) water molecules to measure the microscopic analogue of the macroscopic contact angles on the surface. Each system is equilibrated for at least 500 ps, and typically run by additional 5 ns to secure contact angle convergence. For very hydrophilic surfaces, production runs of up to 10 ns were made. We record the trajectories with 1-ps interval. Contact angles are computed from circular drop contours extrapolated to substrate surface. We use the drop analysis technique developed by de Ruijter et al (5) and described in detail in refs. 6 and 7. To summarize: In each recorded configuration, cylindrical binning was used to get the water drop isochores. Surface normal passing through the center of mass of the droplet is used as the reference axis. The bin thickness is 0.5 Å, and the radial bin boundaries are located at $r_i = (i\delta A/\pi)^{1/2}$ for $1 \le i \le N_{\mathrm{bin}}$ with a base area per bin $\delta A = 50$ Å^2, so that all bins are of equal volume. From the profile, the equimolar dividing surface is determined in each horizontal layer of the binned drop, and a circular fit through these points is extrapolated to the reference plane to measure the contact angle. The z axis position of the reference plane is determined by averaging the effective heights of surface atoms.

As pointed out in ref. 5, the circular contour becomes distorted below the height corresponding to the range of wall-liquid molecular correlation. Above this height, the contour curvature is constant, hence any further increase in the cutoff has no effect on the result. In the present simulations, the empirical cutoff height (satisfying convergence) was typically two or three water diameters above the substrate.

To check for possible droplet size dependence, we also performed runs with water drops containing 4,000 water molecules on 28×28 nm^2 protein-like surfaces, and found no significant differences in contact angles compared to 2,000 molecule drops (Table S2). Further, for methyl-covered substrate, we calculated the wetting free energy of semiinfinite surfaces using planar confinement geometry with lateral periodicity. We used grand canonical Monte Carlo simulations to determine the amount of water between the interfaces. Thermodynamic integration was carried out to obtain the wetting free energy $\Delta\gamma$, and water surface tension, γ, was obtained by the pressure tensor method (8). The Young contact angle $\cos^{-1}(-\delta\gamma/\gamma)$ agreed within 3–5° with the value obtained from the nanodroplet geometry.

The shape of the nanodrop perimeter was found to fluctuate considerably during the simulation, especially when the surface was predominantly hydrophilic. Nonetheless, the long-time averages provided a good fit of circular shapes, and the circular shape was not affected by the patch size, indicating that square lattice patches did not have significant effects on droplet shape.

Local Water Compressibility. To complement the contact angle calculations, we also monitored density fluctuations of interfacial water above our model surfaces. Local water compressibility, κ, can be obtained from density fluctuations:

$$\rho kT\kappa = \frac{\langle N^2\rangle - \langle N\rangle^2}{\langle N\rangle}. \qquad \textbf{[S1]}$$

Here, ρ is the number density and N the number of water molecules in specified volume, k is the Boltzmann constant, T is temperature, and the angular brackets denote the ensemble average. To establish a connection with ref 9, we determined density fluctuations within the solvation layer under the droplets at varied surface compositions. The calculations are done with at least four 400-ps trajectories on each type of the surfaces [mixed -NH_2 and -CH_3 synthetic surface, using AMBER Parm-94 force field (10)]. Only water molecules within 4-Å distance from any surface heavy atom are considered. To discard the effect of fluctuations at the three-phase droplet contour, we considered only the central region of droplet base within 20 Å from the projection of the center of mass of the entire water drop on xy plane. Water compressibility for the whole spectrum of compositions is presented in Fig. S1. Water near hydrophobic surfaces features higher compressibility than near hydrophilic ones. In agreement with refs. 9 and 11 (see also figure 2 in ref 12), the compressibility variation with surface composition (Fig. S1) is especially rapid on hydrophobic surfaces with high fractional solvent-accessible surface (SAS), $f(\mathrm{SAS})_{\mathrm{CH_3}}$. The observed compressibility dependence on $f(\mathrm{SAS})_{\mathrm{CH_3}}$ reaffirms our findings pertaining to extended synthetic surfaces with mixed composition. However, because of nonlinear relation between compressibility and wetting free energy $\Delta\gamma = \gamma\cos\theta_c$, (Fig. S1$C$), the additivity of free energy contributions from distinct mixture component cannot be validated from the compressilibity data.

Force Fields. We compared results obtained by using Lennard–Jones parameters and partial charges of surface groups from three different force fields, CHARMM v27 (14), Amber Parm-94 (10), and OPLS-AA(15) (Table S1). In the main text, we show the results with Amber force fields when -NH_2 groups are involved, because they best reproduced the experiment on -NH_2 functionalized surfaces. Parameters for the nitrile group are available only in OPLS-AA force fields, and we use these when -CN moieties are involved. We mix the small groups on the surfaces with a bias toward alternations, minimizing the number of contacts between surface groups of the same type.

We list the calculated contact angles on pure surfaces (functionalized by groups of a single type) in the bottom of Table S1; we also include experimental water contact angles on self-assembled monolayers with the same end groups (16–19).

The water contact angles on the hydrophobic surfaces (-CH_3) are robust with various force fields, whereas contact angles on hydrophilic (-NH_2) surfaces appear sensitive to the force field choice. In particular, with OPLS-AA force fields, the contact angle of -NH_2 surface is too low compared to the experimental results. This is due to the lack of Lennard–Jones parameters on the hydrogen atoms of -NH_2 groups, allowing water molecules to approach -NH_2 groups too closely. Notwithstanding this differ-

ence, for all three force fields we find similar deviations from linear additivity of $\cos\theta_c$ on mixed -NH_2/-CH_3 surfaces, showing that the interfacial free energy additivity itself is virtually insensitive to force field choice (Fig. S4).

In separate calculations, SPC (20) and TIP3P (21) water models revealed no significant differences in contact angles from those observed with SPC/E(4) water model.

Mixed Surfaces with Uniform Group Polarities. In separate calculations, we confirm that changes in moiety exposures result in strong nonadditivity only when surface functionalities are of different polarities. In Fig. S6 we illustrate the behavior of fictitious systems with reduced partial charges on -CN and -NH_2 groups, making the dipole moments on those groups equivalent to the dipole moments on -CH_3 groups. Surfaces covered by the new artificial groups become hydrophobic, and the deviations of water contact angles from the linear additivity become essentially smaller.

Interfacial Water Structure. ***Distributions of dipole orientations.*** The distribution of water dipole orientations next to the surface covered by equimolar mixture of -CH_3 and -NH_2 groups is very close to that of pure -CH_3 surface and different from that at pure -NH_2 surface (Fig. S3 *Left*). Although the peaks at the mixed -CN/-CH_3 surface are shifted away from the peak position of the pure -CN surface, the average orientation appears to be similar in both cases, in contrast with the behavior of the -NH_2/-CH_3 mixed surfaces.

Perturbation of hydrogen bond network. The perturbations of the hydrogen bonding network can be quantified in terms of the ability of water molecules to maintain tetrahedral coordination. In Fig. S3 *Right*, we plot the distributions of the O-O-O angles of water triplets near various surfaces.

The distribution is defined as follows (23):

$$P\{\cos\theta\} = a\sum_{i=1}^{n_i}\sum_{j=1}^{n_{ij}}\sum_{k<j}\delta\left(\frac{r_{ij}^2+r_{ik}^2-r_{jk}^2}{2|r_{ij}r_{jk}|}-\cos\theta\right), \qquad \textbf{[S2]}$$

where P is the probability, a is the normalization factor, and $r_{\alpha\beta}$ is the distance between water molecules α and β. Here, the sum goes over all water oxygen triplets located within the interface and satisfying O-O distances that permit H-bond formation. We use a geometrical definition of an H bond as described in ref. 24. In pure water, the distribution $P(\cos\theta_{\text{o-o-o}})$ features a broad peak around $\cos\theta_{\text{o-o-o}} \sim -0.3$ when water molecules are forming tetrahedral networks, whereas a small peak at half lower angle corresponds to interstitial water molecules not in tetrahedral formation (25). At the surfaces, the tetrahedral network is partially disrupted with shifts of the large peaks to lower angles (less negative $\cos\theta_{\text{o-o-o}}$); at the same time the interstitial water peaks rise, indicating more water molecules lack tetrahedral coordination. Among all types of surfaces we study, the O-O-O angles' peak shift is most pronounced at the surface covered by -CN groups (indigo curve in Fig. S3 *Right*), consistent with our observation of the reduction in the average number of hydrogen bonds of water molecules near that surface (Fig. 2*B* in main text). We note that, by limiting the statistics to water triplets with O-O distances within the hydrogen bond length of up to 3.5 Å, a larger fraction of water molecules outside the hydrogen bonded network remain unaccounted for. Inclusion of these water molecules would enhance the measured extent of the disruption of tetrahedral coordination in interfacial water.

Dependence of Surface Hydration on Composition. The composition dependence of $\cos\theta_c$ on mixed -CH_3/-NH_2 surfaces shown in Fig. 1 *Right* and Fig. S4 *Left*, plotted with no correction of surface-accessible areas, features a rapid change around $f_{CH_3} \sim 0.4$. To verify if this change can be related to a structural reorganization of liquid interface, in Fig. S2 we present water coordination numbers $N_c(4\text{ Å})$ (number of water molecules per unit area in the first solvation layer of the graphene substrate, $2.8\text{ Å} \le z \le 4\text{ Å}$ from graphene atoms) over the whole range of the fraction of methyl groups, f_{CH_3}. Consistent with Fig. 2*A*, we observe considerable penetration of water between planted groups on surfaces dominated by amino groups, but water is rapidly displaced with increasing f_{CH_3}. At $f_{CH_3} \sim 0.4$, only about one-third of the original amount of water is left in the first hydration shell, and the slope of $N_c(f_{CH_3})$ is slowed down; however, the change is gradual over the whole range of f_{CH_3}.

Account of Relative Roughnesses on a Mixed Surface in the Original Cassie's Equation. Uneven exposures of surface components, quantified in terms of relative roughnesses, can be captured by the original Cassie's equation, Eq. **1** in the main text: $\cos\theta_c = f_A r_A \cos\theta_A + f_B r_B \cos\theta_B$. At the molecular level, the Wenzel roughness factors r_α (26) can be expressed as the ratios of solvent-accessible (exposed) areas $A(\alpha)$ of a patch of type α in the mixture and that of a pure-surface fragment of equal projected area, $r_\alpha = A(\alpha)_{\text{SAS(mix)}}/A(\alpha)_{\text{SAS(pure)}}$. Fig. S5 illustrates a qualitative agreement between the simulated cosines of contact angles for mixed synthetic surfaces (solid red symbols) and predictions obtained using the above additivity relation (Eq. **1** from the main text) along with SAS-based roughness parameters r_α (open blue symbols).

Protein Surface. The protein flattening procedure is adapted from Giovambattista et al. (27). As in that work, we use the CHARMM v27 (14) force field, which is widely accepted in reproducing the bonding and nonbonding properties of biological systems. The electrostatic potential maps were calculated with APBS program (28), in analogy with ref 27.

For all three types of building blocks of protein surfaces (type A, B, and C described in the main text), the simulated contact angles depend very weakly on the replication method; the difference between contact angles on periodic surfaces and surfaces with randomized patch orientations was approximately 2°. For hydrophilic surface types (A and C), the averaged results have bigger standard deviations because the water drop spreads over a large part of the surface, making an accurate determination of the contact angle more difficult. The water contact angles (2,000 water molecules per drop) measured on periodically replicated and randomized flattened protein surfaces are collected in Table S2.

On a nonuniform surface, a droplet may prefer to cover hydrophilic patches at the expense of hydrophobic ones. To verify whether this is the case on mixed protein-like surfaces, we determined two quantities: (*i*) the number of water molecules above hydrophilic and hydrophobic patches within the central region of the droplet on a mixed surface with symmetric (50/50% A/B) composition, and (*ii*) the average composition of total wetted area under the drop as a function of the composition of the whole substrate. Fig. S7 *Left* illustrates water distributions above hydrophilic (A) and hydrophobic (B) patches, sampled inside the central 15% of the drop's projected area (area within 2 nm from drop's central axis, extending over 3–4 surface patches) for a drop on a symmetrically mixed A/B surface. These results show that the drop's center spends more time atop hydrophilic domains. The total area under the drop, however, includes many patches of both types (>20 patches in the case of symmetric A/B mixture). Our results presented in Fig. S7 *Right* show the average surface compositions of the wetted area under the simulated drop are consistently close to the composition of the whole substrate.

1. Plimpton S (1995) Fast parallel algorithms for short-range molecular-dynamics. *J Comput Phys* 117:1–19.
2. Evans DJ, Holian BL (1985) The Nose–Hoover thermostat. *J Chem Phys* 83:4069–4074.
3. Darden T, York D, Pedersen L (1993) Particle mesh Ewald—An N.Log(N) method for Ewald sums in large systems. *J Chem Phys* 98:10089–10092.
4. Berendsen HJC, Grigera JR, Straatsma TP (1987) The missing term in effective pair potentials. *J Phys Chem* 91:6269–6271.
5. de Ruijter MJ, Blake TD, De Coninck J (1999) Dynamic wetting studied by molecular modeling simulations of droplet spreading. *Langmuir* 15:7836–7847.
6. Werder T, Walther JH, Jaffe RL, Halicioglu T, Koumoutsakos P (2003) On the water-carbon interaction for use in molecular dynamics simulations of graphite and carbon nanotubes. *J Phys Chem B* 107:1345–1352.
7. Daub CD, Bratko D, Leung K, Luzar A (2007) Electrowetting at the nanoscale. *J Phys Chem C* 111:505–509.
8. Bratko D, Daub CD, Leung K, Luzar A (2007) Effect of field direction on electrowetting in a nanopore. *J Am Chem Soc* 129:2504–2510.
9. Acharya H, Ranganathan S, Jamadagni SN, Garde S (2010) Mapping hydrophobicity at the nanoscale: Applications to heterogeneous surfaces and proteins. *Faraday Discuss* 146:353–365.
10. Cornell WD, et al. (1995) A second generation force-field for the simulation of proteins, nucleic acids, and organic molecules. *J Am Chem Soc* 117:5179–5197.
11. Bratko D, Daub CD, Luzar A (2009) Water-mediated ordering of nanoparticles in an electric field. *Faraday Discuss* 141:55–66.
12. (2010) General Discussion. *Faraday Discuss* 146:367–393.
13. Shrake A, Rupley JA (1973) Environment and exposure to solvent of protein atoms—Lysozyme and insulin. *J Mol Biol* 79:351–371.
14. MacKerell AD, et al. (1998) All-atom empirical potential for molecular modeling and dynamics studies of proteins. *J Phys Chem B* 102:3586–3616.
15. Jorgensen WL, Maxwell DS, TiradoRives J (1996) Development and testing of the OPLS all-atom force field on conformational energetics and properties of organic liquids. *J Am Chem Soc* 118:11225–11236.
16. Keselowsky BG, Collard DM, Garcia AJ (2003) Surface chemistry modulates fibronectin conformation and directs integrin binding and specificity to control cell adhesion. *J Biomed Mater Res, A* 66A:247–259.
17. Sigal GB, Mrksich M, Whitesides GM (1998) Effect of surface wettability on the adsorption of proteins and detergents. *J Am Chem Soc* 120:3464–3473.
18. Bain CD, Evall J, Whitesides GM (1989) Formation of monolayers by the coadsorption of thiols on gold—Variation in the head group, tail group, and solvent. *J Am Chem Soc* 111:7155–7164.
19. Arima Y, Iwata H (2007) Effect of wettability and surface functional groups on protein adsorption and cell adhesion using well-defined mixed self-assembled monolayers. *Biomaterials* 28:3074–3082.
20. Berendsen HJC, Postma JPM, van Gunsteren WF, Hermans J (1981) *Intermolecular Forces* ed Pullman B (Reidel, Dordrecht, The Netherlands), p 331.
21. Jorgensen WL, Chandrasekhar J, Madura JD, Impey RW, Klein ML (1983) Comparison of simple potential functions for simulating liquid water. *J Chem Phys* 79:926–935.
22. Cassie ABD (1948) Contact Angles. *Discuss Faraday Soc* 3:11–16.
23. Daub CD, Leung K, Luzar A (2009) Structure of aqueous solutions of monosodium glutamate. *J Phys Chem B* 113:7687–7700.
24. Luzar A, Chandler D (1993) Structure and hydrogen bond dynamics of DMSO-water mixtures by computer simulations. *J Chem Phys* 98:8160–8173.
25. Soper AK, Castner EW, Luzar A (2003) Impact of urea on water structure: A clue to its properties as a denaturant? *Biophys Chem* 105:649–666.
26. Wenzel RN (1936) Resistance of solid surface to wetting by water. *Ind Eng Chem* 28:988–994.
27. Giovambattista N, Lopez CF, Rossky PJ, Debenedetti PG (2008) Hydrophobicity of protein surfaces: Separating geometry from chemistry. *Proc Natl Acad Sci USA* 105: 2274–2279.
28. Baker NA, Sept D, Joseph S, Holst MJ, McCammon JA (2001) Electrostatics of nanosystems: Application to microtubules and the ribosome. *Proc Natl Acad Sci USA* 98: 10037–10041.

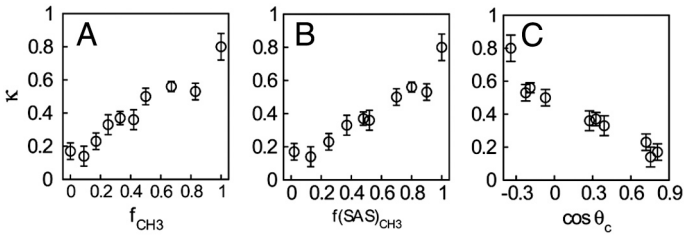

Fig. S1. Water compressibility (in arbitrary units) next to surfaces with different fraction of hydrophobic groups (*y* axis); *x* axis represents the mole fraction of -CH_3 groups on surfaces in *A*, hydrophobic fractional area in terms of SAS (13) in *B*, and cosine of contact angle in *C*. Error bars are obtained as standard error in the mean.

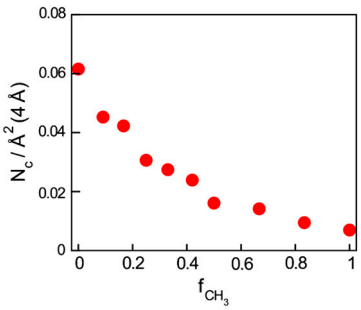

Fig. S2. Coordination numbers $N_c(z)$ on mixed -CH_3/-NH_2 surfaces at $z = 4$ Å from the bottom surface.

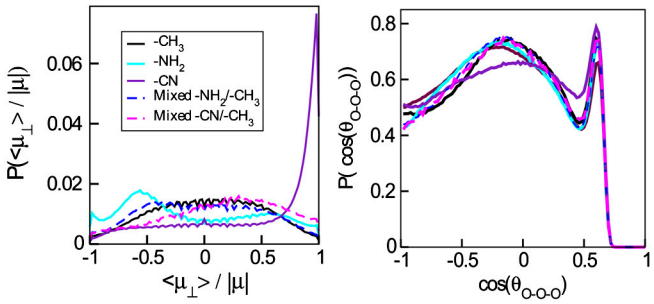

Fig. S3. (*Left*) Distribution of dipole orientation at the graphite surfaces functionalized by different head groups. (*Right*) Distribution of O-O-O angles in triplets of water molecules (defined in Eq. **S2**).

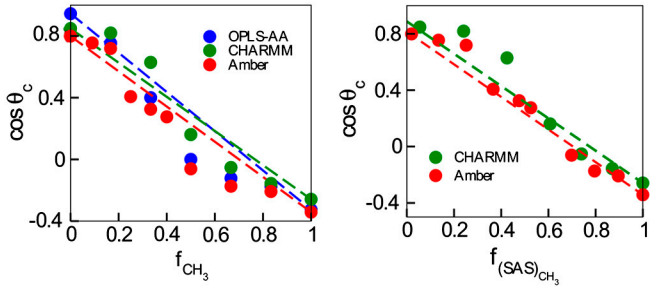

Fig. S4. (*Left*) Cosine of contact angles on mixed -CH_3/-NH_2 surfaces as a function of the mole fraction of substrate surface covered by -CH_3. The dashed lines are the Cassie prediction (22), Eq. **2** in the main text, for all the force fields we tested in our studies. (*Right*) Cosine of contact angles on mixed -CH_3/-NH_2 surfaces as a function of the fraction of surface defined by SAS, covered by -CH_3, with both CHARMM and Amber force fields. Squares, simulation results for bigger 4×4 headgroup patches in equimolar mixtures.

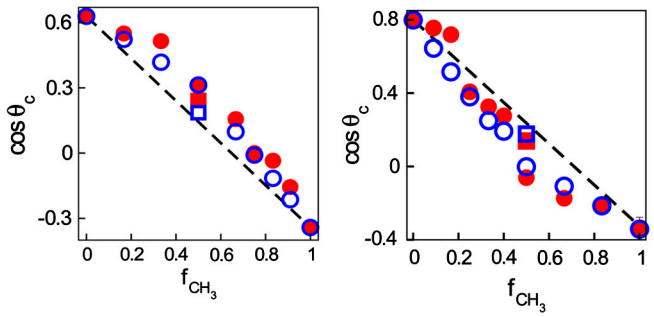

Fig. S5. Simulated cosines of contact angles (solid red symbols) on mixed -CH_3/-CN (*Left*) and -CH_3/-NH_2 surfaces (*Right*) as functions of the mole fraction of -CH_3 groups on the substrate surface. Solid circles, simulation results for molecularly mixed surfaces; open squares, results obtained with 4×4 headgroup patches. The dashed lines are the simplified Cassie prediction (22) (Eq. **2** in the main text). Open blue symbols are calculated by the original Cassie equation (Eq. **1** in the main text) with factors r_α obtained from changes in solvent-accessible areas.

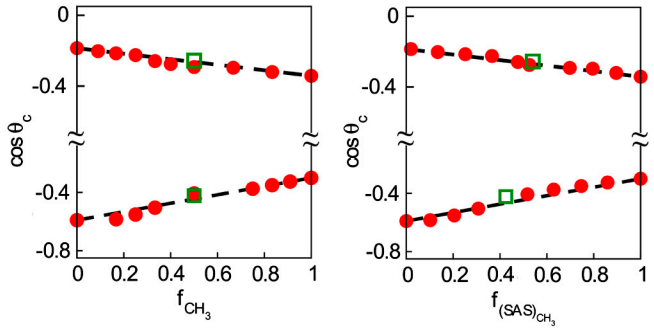

Fig. S6. Water contact angle on surface groups with artificially reduced partial charges. (*Left*) Cosine of contact angles on mixed -CH_3/-"NH_2" surfaces (*Upper*) and -CH_3/"-CN" (*Lower*) as a function of the mole fraction of substrate surface covered by -CH_3. The dashed lines are the Cassie prediction (22) (Eq. **2** in the main text). (*Right*) Cosine of contact angles on mixed -CH_3/-"NH_2" surfaces (*Upper*) and -CH_3/"-CN" (*Lower*) as a function of the fraction of surface defined by SAS, covered by -CH_3.

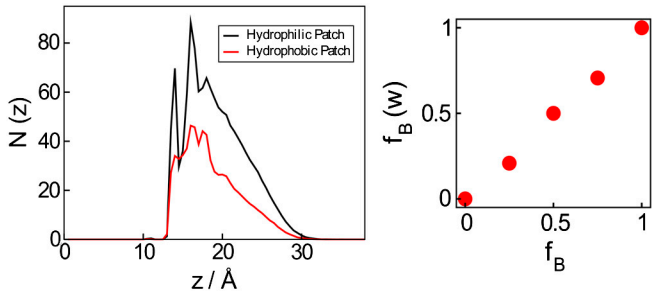

Fig. S7. (*Left*) Distributions of water molecules inside the central region ($r \leq 2$ nm) of a 2,000-molecule droplet of radius $r \sim 5$ nm on a symmetrically mixed protein surface with hydrophilic (*A*) and hydrophobic (*B*) patches indicating preferential positioning of the drop's center above hydrophilic patches. $N(z)$ is the number of water molecules in slabs $z \pm 0.5$ Å located above hydrophilic (black) or hydrophobic (red) patches. Note also the comparatively loose liquid interface on hydrophobic domains. (*Right*) Average composition of the total wetted area under the droplet, $f_B(w)$, resembles the overall composition of the surface, f_B, over the whole range $0 \leq f_B \leq 1$.

Table S1. Force fields used for surfaces head groups and contact angle results

Atom		$\sigma_{A\text{-}O}$(Å)	$\epsilon_{A\text{-}O}$(kcal/mol)	Partial charge, e
C (Graphene) (6)		3.214	0.0361	0
OPLS-AA (ref. 15)				
C(-CH_3)		3.5	0.066	−0.18
H(-CH_3)		2.5	0.03	0.06
N(-NH_2)		3.25	0.17	−0.7
H(-NH_2)		—	—	0.35
C(-CN)		3.3	0.066	0.46
N(-CN)		3.2	0.17	−0.46
Amber (ref. 10)				
C(-CH_3)		3.816	0.1094	−0.18
H(-CH_3)		2.974	0.0157	0.06
N(-NH_2)		3.648	0.17	−0.84
H(-NH_2)		1.2	0.0157	0.42
CHARMM (ref. 14)				
C(-CH_3)		3.670	0.08	−0.27
H(-CH_3)		2.352	0.022	0.09
N(-NH_2)		3.296	0.2	−0.80
H(-NH_2)		0.4	0.046	0.40
Contact angles on homogeneous surfaces				
	OPLS-AA	CHARMM	Amber	Experimental
-CH_3	109°	106°	109°	107° (16)/112° (17)
-NH_2	18°	32°	36°	43° (16)/50° (19)
-CN	50°	-	-	61° (18)/63° (17)

Table S2. Water contact angle on protein-like surfaces with large patches

Drop size dependence			
Water nanodrop	type A	50/50 A/B	type B
2,000 molecules	20° ± 4°	46° ± 2°	113° ± 1°
4,000 molecules	18° ± 3°	48° ± 2°	115°± 1°
Dependence on the method of patch replication			
2,000 molecules	periodic		randomized
Type A	22° ± 3°		20° ± 4°
Type B	115° ± 1°		113° ± 1°
Type C	20° ± 3°		18° ± 2°